

# An Investigation of Process Parameter Modifications on Additively Manufactured Inconel 718 Parts

Christopher Kantzos, Joseph Pauza, Ross Cunningham, Sneha P. Narra, Jack Beuth, and Anthony Rollett

(Submitted March 23, 2018; in revised form July 20, 2018; published online September 4, 2018)

**Additive manufacturing (AM) allows for the fabrication of complex parts via layer-by-layer melting of metal powder. Laser powder-bed AM processes use a variety of process parameters including beam power, beam velocity, and hatch spacing to control melting. Alterations to these parameters have often been attempted to reduce porosity, for example, but less work has been done to on comprehensive effects of process parameter modifications. This study looks at the effects of altering these parameters on microstructure, porosity, and mechanical performance of Inconel 718. The results showed that process parameter modifications that result in porosity formation can significantly reduce fatigue life, while microstructure changes were minimal and had little effect on tensile properties. The precipitate structure was not found to be changed significantly. These results can inform future process parameter modifications, as well as heat treatments to optimize mechanical properties.**

**Keywords** additive manufacturing, Inconel 718, mechanical properties, microstructure, process parameters, selective laser melting

is expected to provide more complete control to manufacturers and users alike.

## 1. Introduction

Process parameter modifications in powder-bed additive manufacturing (AM) have been shown to have a large effect on material/manufacturing concerns such as porosity (Ref 1), surface roughness (Ref 2), and melt pool geometry (Ref 3). Inconel 718 is a nickel-based superalloy that has received a tremendous attention in AM (Ref 4-7), particularly because many of the industries that intend to implement AM in their production have high-temperature applications well suited to superalloys. Inconel 718 is also one of the most common, and most easily weldable superalloys (Ref 8), making it ideal for AM. While most of the research to date on process parameter modifications has focused on reducing undesired features such as porosity (Ref 1), little work has been performed on microstructure optimization (e.g., microstructure refinement) (Ref 9). A particular focus of this study was the exploration of process parameter space within the normal operating range, as opposed to determining the limits. Using the combined insight from the literature, a study was completed to look at the effects of four process parameter modifications, considering the effects on microstructure, porosity, and mechanical properties, which

## 2. Experimental

The samples in this study were manufactured using standard IN 718 powder (20-63  $\mu\text{m}$ ) with an EOS M290 system in an argon atmosphere using virgin powder with a layer thickness of 40  $\mu\text{m}$ . A total of five process parameter sets were used, namely the EOS standard parameter set and 4 modifications. A previous study on Ti64 showed that decreasing the hatch spacing below the value used in the standard parameter set resulted in reduced amounts of trapped gas porosity in the build (Ref 10). This suggests that deviations from the standard set of parameters can result in builds tailored with different objectives in mind, for example minimal porosity formation or maximized build rate. The choice of process parameters was based on the mapping of results from a series of single beads fabricated without powder (e.g., laser tracks on an IN 718 plate). Standard parameters (set 1) include a power of 285 W, a velocity of 960 mm/s, and a hatch spacing of 110  $\mu\text{m}$ . The corresponding single-bead experiments gave a melt pool width of 163  $\mu\text{m}$  and a calculated minimum depth of melted material between beads of 58 microns for this case. Tang et al. (Ref 11) showed that a geometric model could be used to predict lack of fusion porosity, so the parameter sets were developed with this in mind with the objective of determining whether lack of fusion porosity could be controlled in a similar way in this material system. Parameter sets 2 and 3 were designed to change the hatch spacing by increasing it to 150  $\mu\text{m}$  and decreasing it to 80  $\mu\text{m}$ , respectively. The larger hatch spacing was designed to introduce a controlled increase in lack of fusion porosity by decreasing the minimum depth of melting to 31  $\mu\text{m}$  (which is less than the layer thickness of 40  $\mu\text{m}$ ). The smaller hatch spacing was chosen to reduce the likelihood of porosity from lack of fusion by increasing the minimum melting depth to 68  $\mu\text{m}$  and to reduce the likelihood of porosity from the powder, by increasing remelting and allowing more opportunity

This article is an invited paper selected from presentations at the symposium “Additive Manufacturing of Metals: Microstructure and Material Properties,” held during MS&T’17, October 8-12, 2017, in Pittsburgh, Pa., and has been expanded from the original presentation.

**Christopher Kantzos, Joseph Pauza, Ross Cunningham, and Anthony Rollett**, Materials Science and Engineering, Carnegie Mellon University, Pittsburgh, PA, USA; and **Sneha P. Narra and Jack Beuth**, Mechanical Engineering, Carnegie Mellon University, Pittsburgh, PA, USA. Contact e-mail: rollett@andrew.cmu.edu.

for powder porosity to “bubble out” of the melt pool. Ideally, this should result in decreased porosity levels albeit at the cost of lower build rate. Parameter sets 4 and 5 were selected to observe the effect of alterations of cooling rate. Parameter set 4 was selected to increase the solidification cooling rate in the build by a factor of roughly 1.2 (by decreasing melt pool size) while still avoiding lack of fusion porosity caused by small melt pools. Its minimum melt depth is still 58  $\mu\text{m}$  through a decrease in hatch spacing. Parameter set 5 was selected to lower the cooling rate of the build by a factor of roughly 0.65 by increasing melt pool size. In this case, the hatch spacing was also increased to yield a minimum melting depth of 58  $\mu\text{m}$ . However, in an attempt to decrease cooling rate as much as possible, this case was chosen to be slightly into the large melt pool region of processing space where keyholing (local vaporization of the melt pool) was observed in the single-bead tests. Results from later in this paper will show that this case actually yielded substantial keyholing porosity in solid builds. Parameter sets are illustrated in Table 1.

In order to explore the microstructural effects of the altered parameters, a heat treatment was used that did not result in recrystallization of the as-built solidification microstructure. Intended to mirror AMS 2774A (Ref 12), this heat treatment was performed in an argon atmosphere and consisted of a purge for 15 min followed by a ramp up to 968 C at 20 C/min. The samples were held at 986 C for 1 h before the furnace was ramped down to 718 C at  $-1$  C/min where the samples were

held for 9 h. The furnace was then ramped down again, this time to 621 C at  $-1$  C/min. The samples were held here for 10 h before being ramped down to room temp at a rate of  $-1$  C/min.

Tensile and fatigue tests were completed to evaluate the effects of the different processing parameters on mechanical response. The tensile specimens were built in accordance with ASTM designation E8/E8M (Ref 13), with a printed gage section diameter of 0.575” machined down to 0.5” and a gauge length of 2”. The tensile specimens were all built vertically such that the loading direction is parallel to the build direction. The fatigue specimens were designed and printed in accordance with ASTM designation E466 (Ref 14). The specimens possessed a 1.25” long gage section with a printed diameter of .289”. All specimens were machined down 1 mm in diameter to eliminate the near-surface microstructure from contour passes and the ends of rasters. The fatigue specimens were also built with the loading and build directions aligned in parallel. Tensile testing was completed with a strain rate of  $0.01\text{ s}^{-1}$ . Fatigue testing was completed on a load frame with hydraulic collet grips, in load control, with a maximum stress of 827.4 MPa,  $R$  ratio of 0, and frequency of 30 Hz. All mechanical testing was completed at 25 °C.

Microscopy was completed on a FEI Quanta 600, with samples polished to a 0.05- $\mu\text{m}$  finish. Synchrotron-based micro-computed tomography ( $\mu\text{SXCT}$ ) was completed at the Advanced Photon Source 2BM beamline, reconstructions were

**Table 1** Parameter set information

Parameter	Power, W	Velocity, mm/s	Hatch spacing, $\mu\text{m}$	Modification
1	285	960	110	Nominal parameters
2	285	960	150	Increased hatch spacing
3	285	960	80	Decreased hatch spacing
4	300	1200	80	Increased cooling rate
5	200	400	180	Decreased cooling rate

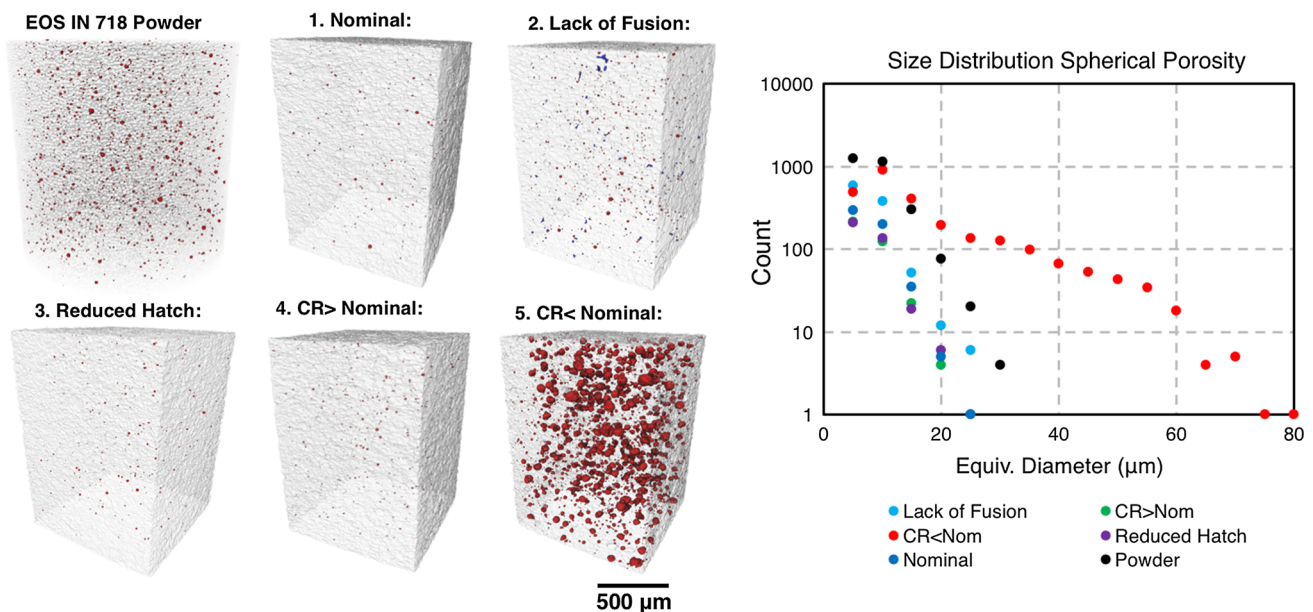


**Fig. 1** Results of CT scans for the parameter sets. On the left is the image of the porosity for 5 parameter sets, and on the right is the pore size count plots, taken over a volume of approximately  $1\text{ mm}^3$ . It is apparent parameter set 5 which has much more porosity than the other parameter sets, which all had lower porosity than the powder

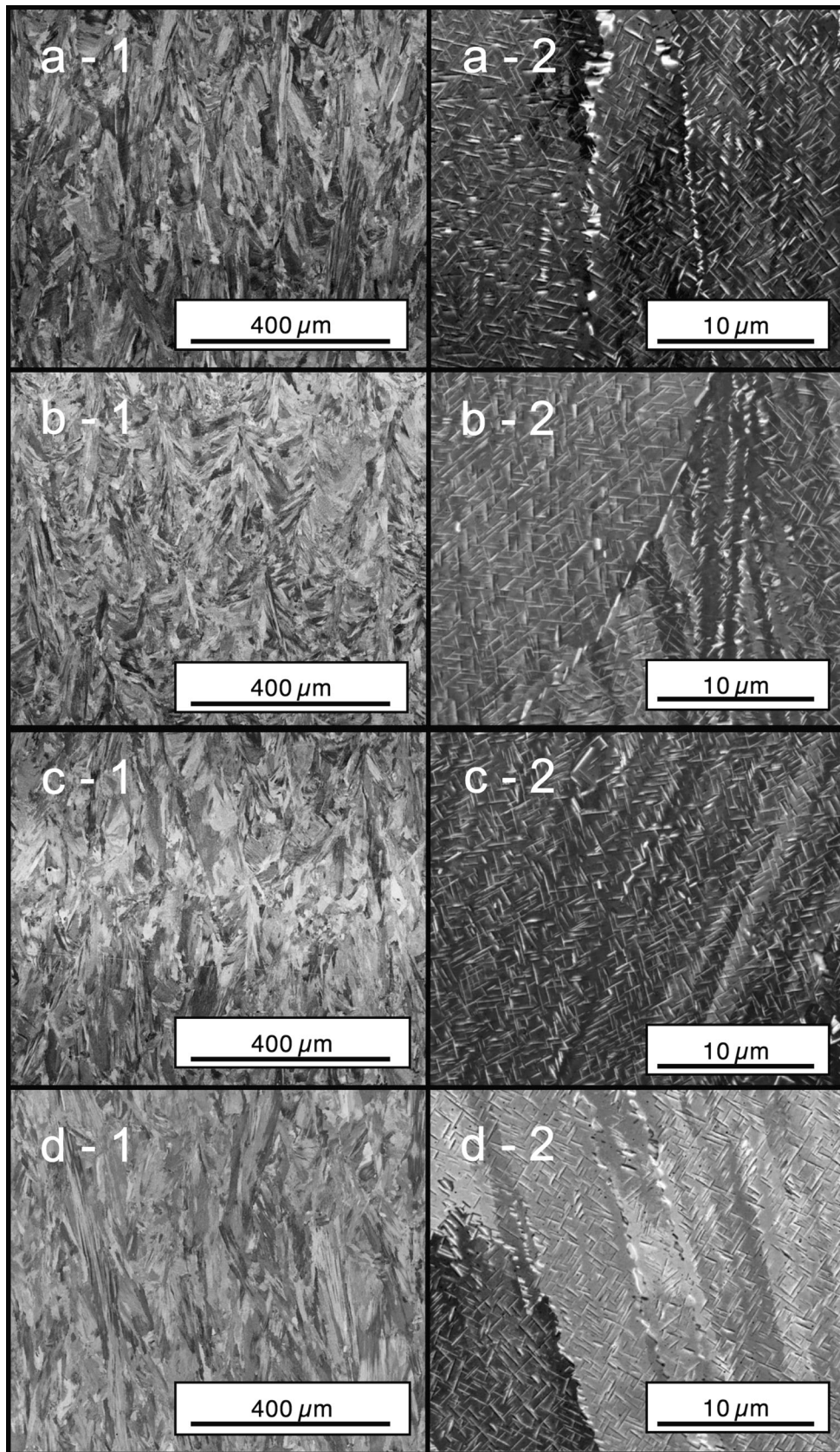


**Fig. 2** Microstructure images of parameter sets 1 (a), 2 (b), 3 (c), and 4 (d). The 1 corresponds to a magnification of  $\times 149$ . The 2 corresponds to a magnification of  $\times 4758$

completed using Tomopy (Ref 15), and visualizations were completed using Avizo™. Samples were prepared for CT by being cut from the center of the fatigue bars using electrical discharge machining (EDM) to be 1 mm × 1 mm × 25 mm (Fig. 1).

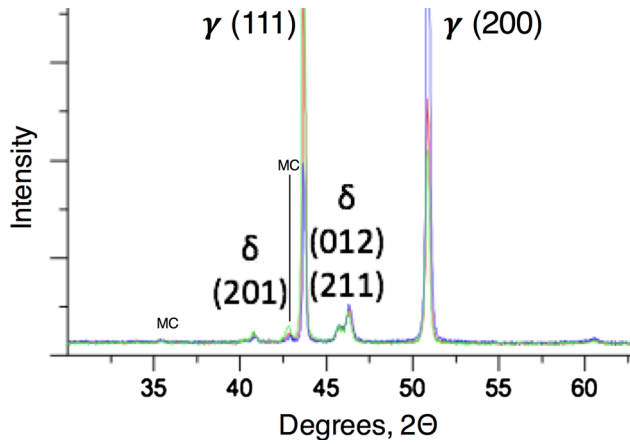


Fig. 3 XRD of parameter sets 1, 2, and 4 overlaid on each other

### 3. Results and Discussion

#### 3.1 Porosity

The  $\mu$ SXCT scans from the 2BM beamline have a voxel size of 0.65  $\mu$ m, resulting in a  $\sim$  1.5- $\mu$ m feature resolution. The raw reconstructions were manually thresholded based on intensity and visualized using Avizo. Figure 2 shows the images of the porosity on the left, and the number density plot of the porosity on the right. The porosity was randomly distributed throughout the builds. The most apparent result was that parameter set 5 had significantly more and larger porosity than the other data sets. Again, results from single-bead tests with no powder suggested that some keyholing porosity was possible for this case, but the amount of large, spherical keyhole porosity was more than expected. The second largest amount of porosity was seen in the powder, suggesting the rest of the parameters efficiently reduced the porosity transferred from the powder. Of the remaining parameter sets, it is notable that parameter set 2 (increased hatch spacing/lack of fusion) did have a noticeable increase in small spherical porosity from the powder and a small amount of large, irregularly shaped pores from lack of fusion. The remaining parameter sets were mostly indistinguishable, though the reduced hatch case showed slightly less porosity from the powder. This suggests that the nominal parameters were already very effective in reducing the transfer of powder porosity to the specimens, so the increased remelting

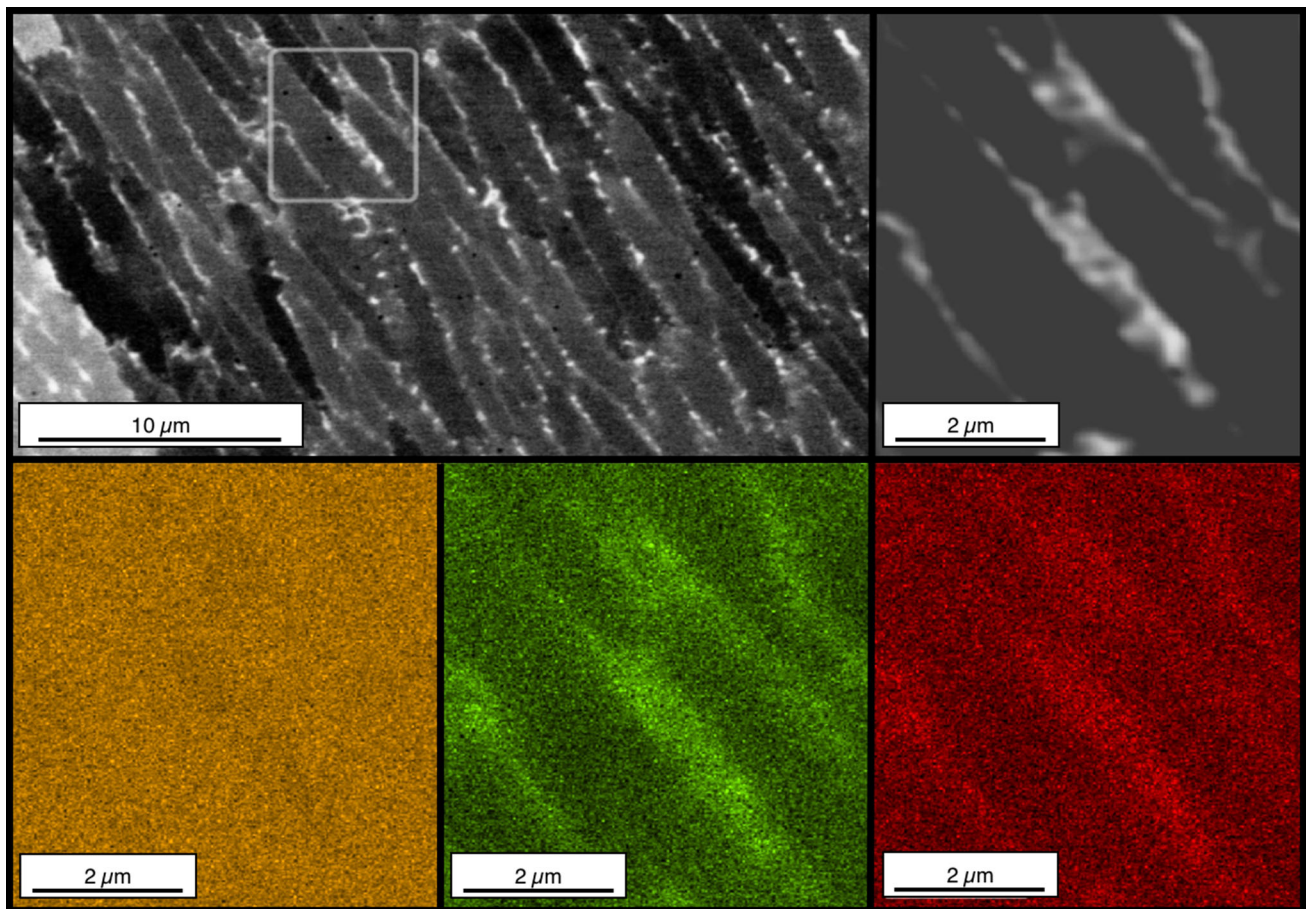
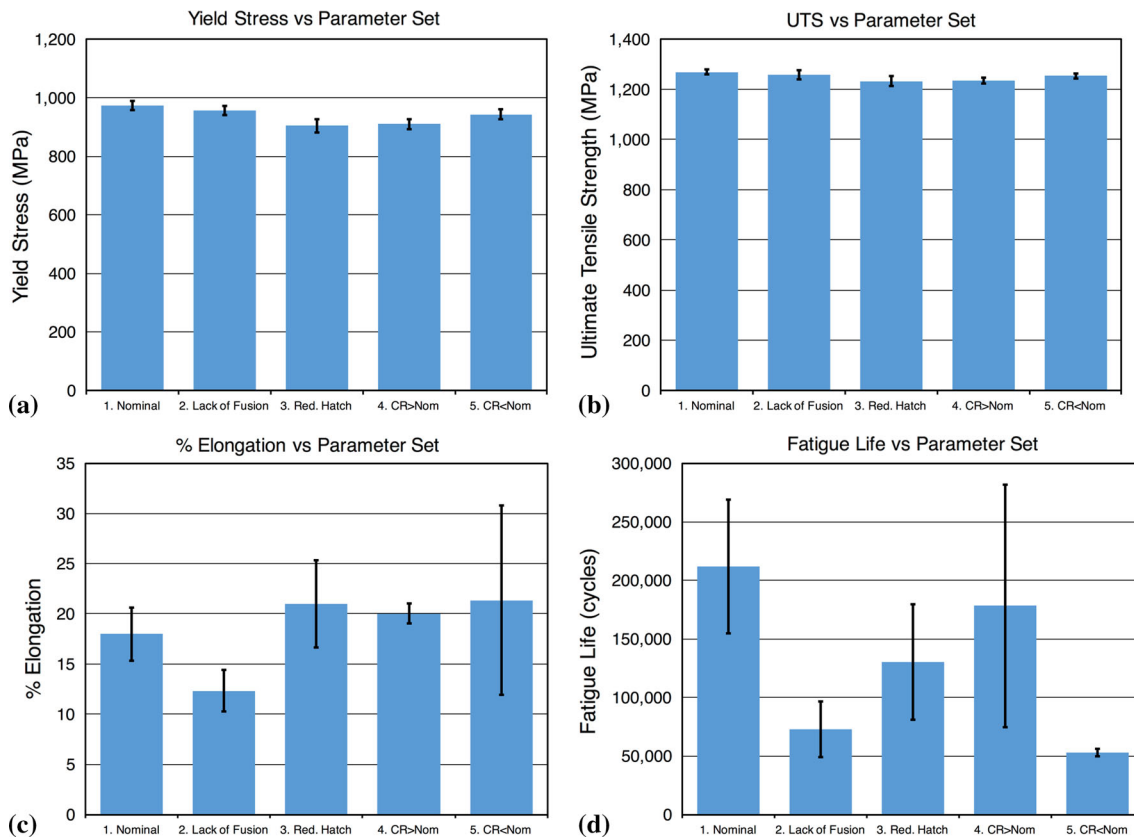


Fig. 4 Micro-segregation in the as-built Inconel 718 samples



**Fig. 5** Bar plots showing the averages for tensile properties (a-c) and fatigue lives (d) for the different parameter sets

from the reduced hatch spacing did not offer a significant added benefit.

### 3.2 Microstructure Analysis

The bulk microstructure of each parameter set was investigated in order to observe microstructure differences as a result of parameter alterations. Figure 3 shows images of the bulk microstructure for parameter sets 1, 2, 3, and 4 taken with an FEI Quanta 600 located in the Carnegie Mellon Materials Characterization Center. Qualitative analysis of the microstructures shows some differences in grain structure, namely for parameter set 2 which is the most “equiaxed” of the cases. This is likely because the larger hatch spacing resulted in less remelting, which led to fewer opportunities for epitaxial growth to occur, and also the sides of the melt pools were retained.

The higher magnification images on the right show the precipitates for the chosen parameter sets. No noticeable differences exist between the precipitate size and spacing. While analysis of traditionally manufactured (e.g., wrought) Inconel 718 is noted to have a platelike  $\gamma''$  precipitates, with a noted orientation relationship similar to what is seen here (Ref 14), certain studies have suggested for AM Inconel 625 (Ref 15) and for AM Inconel 718 (Ref 16) these platelike precipitates are actually the  $\delta$  phase. This motivated the use of x-ray diffraction (XRD) to analyze the main phases in the microstructure. Figure 4 shows the  $2\theta$  plot for the XRD scan for the Inconel 718. The primary peaks are noted to be the main  $\gamma$  phase, with smaller peaks noted to be  $\delta$  phase. Lass et al. (Ref 16) found similar peaks in Inconel 625 and showed (using local synchrotron diffraction) that this disk-shaped bulk precipitate is

actually  $\delta$  phase and not the anticipated  $\gamma''$  phase. The proposed mechanism for this  $\delta$  formation is segregation of niobium (the main constituent in  $\gamma''$  and  $\delta$ ) to the cell boundaries during solidification. To examine this with more details, a sample of Inconel 718 that was as-built was imaged in the SEM to reveal the as-solidified structure. Figure 5 shows a high-resolution ( $\sim 5000\times$ ) image of the as-built material, where obvious solidification segregation has occurred. An energy-dispersive x-ray spectroscopy (EDS) map is also shown in Fig. 5 that reveals the segregated material is niobium. This suggests the segregation of niobium leads to the early formation of  $\delta$  which was coarsened during the heat treatment, all of which is in agreement with what was described by Lass et al. (Ref 16).

### 3.3 Mechanical Testing

Tensile testing was completed for three samples from each parameter set. Figure 5 shows the averages for the 0.2% yield stress, ultimate tensile strength, and % elongation in sections (a), (b), and (c), respectively. The fatigue tests were all run under the same conditions, listed in section 3, and the resulting fatigue lives are shown in Fig. 4(d). The tensile properties for the different parameter sets showed only minor differences in strength and elongation. The strength values are similar to those found by Zhao et al. (Ref 17) for AM Inconel 718 when looking at as-built microstructures; however, the present work shows slightly higher strength due to the heat treatment applied in the samples shown in Fig. 4. Zhao et al. (Ref 17) also showed that a recrystallized microstructure produced tensile strengths much closer to wrought Inconel 718 (Ref 18). The overall spread of the tensile results between the altered process

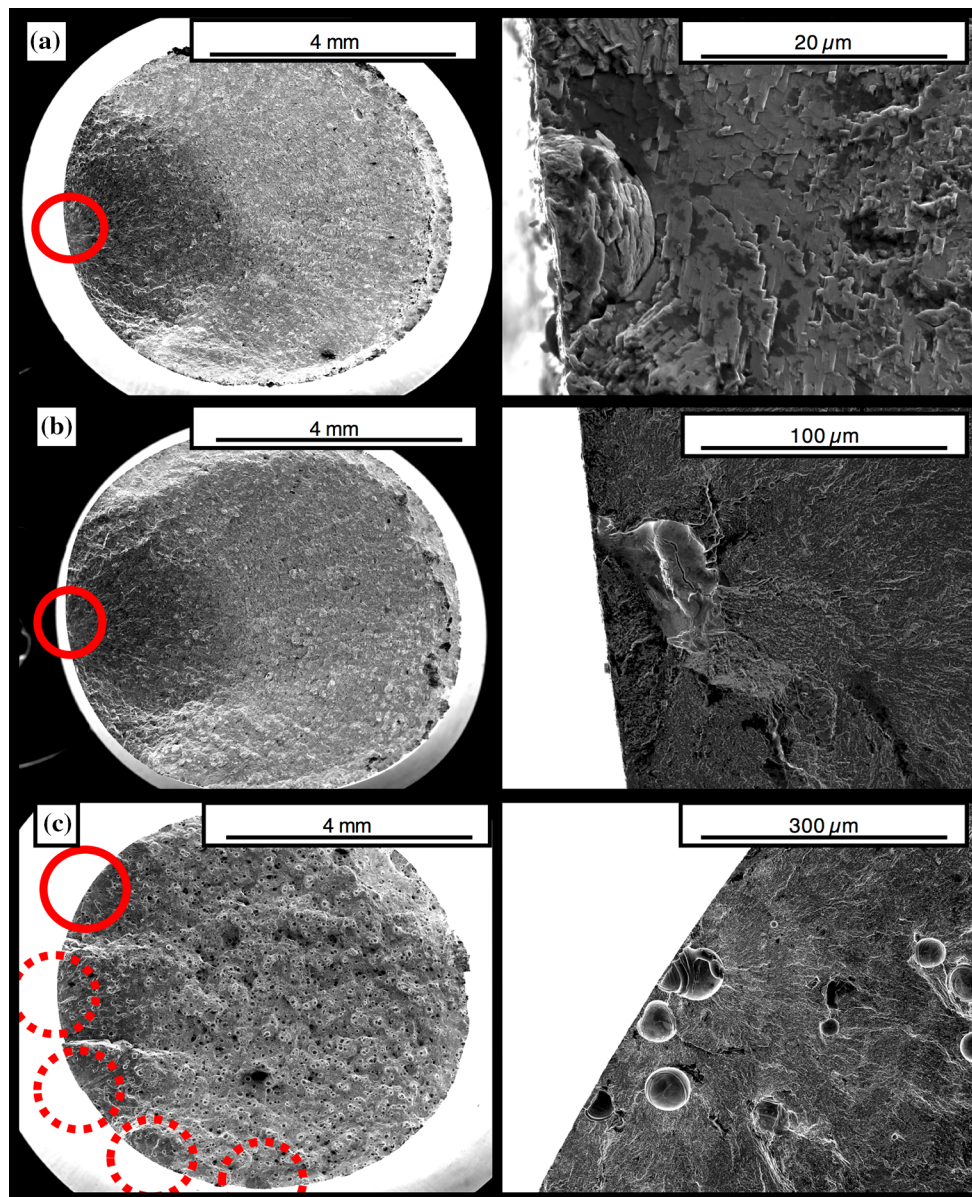


**Fig. 6** Fracture surfaces at two different magnifications for parameter sets 1 (a), 2 (b), and 5 (c), showing at low magnification the number of initiations (circled in red, and at high magnifications the initiation site

parameters is small, leading to the observation that the altered parameters provided little effect on the overall strength of the material. Rather, the large size of the  $\delta$  phase [compared to the traditionally observed fine  $\gamma''$  phase (Ref 14)], was observed in each part regardless of processing parameters. This is likely the cause of the decreased strength of the heat-treated Inconel 718 in this study.

The fatigue data showed much greater variation in results than the tensile tests, indicating that the altered processing parameters did have an impact on the fatigue life. Figure 5(d) shows the results of the fatigue tests. Parameter sets 2 and 5 showed significantly reduced fatigue life. These parameter sets correspond to the lack of fusion samples and the slow cooling rate samples, respectively. It is reasonable to conclude that the increased porosity generated by the selected parameter sets caused the premature failure observed in these samples. This is true even for the lack of fusion parameter set 2, which had only

a small amount of lack of fusion flaws. Figure 6 shows the fracture surfaces for process parameter sets 1, 2, and 5. The nominal parameters (set 1) had an initiation site from a small pore on the surface, while the fracture surface for set 2 shows a large lack of fusion pore and parameter set 5 shows multiple initiation sites at or near the surface due to the large amount of porosity present in the sample.

#### 4. Conclusions

Alterations in the processing parameters of the EOS M290 to build Inconel 718 parts and the impact these alterations had on microstructure and mechanical properties were investigated. The microstructures of each process parameter set revealed small changes in grain morphology and no noticeable change in

the large amounts of  $\delta$  phase in both the grain boundary and the bulk. Porosity analysis showed that the increase in hatch spacing and the slower cooling rate resulted in increased porosity.

Tensile test results revealed that the microstructure changes and porosity differences did not significantly affect strength, but fatigue test results showed that the parameter sets with increased porosity (2 and 5) resulted in significantly reduced fatigue life, while the microstructural changes did not seem to affect fatigue life. Applications where monotonic tensile strength is the only requirement may benefit from process parameter alterations, particularly where build rate is considered critical. Both precipitation formation in the microstructure of additively manufactured Inconel 718 and the defect formation as a result of process parameters can have a significant impact on part performance. Optimization of both aspects of Inconel 718 AM builds is critical to ensuring optimal part performance.

Parameter set 3 was designed with the goal of reducing porosity by decreasing the hatch spacing. The decreased hatch spacing in set 3 did not produce the reduced porosity levels compared to the nominal parameters as observed in other material systems. The negative effects of this porosity were apparent in the shorter fatigue lives.

## Acknowledgments

The authors acknowledge the support of the NextManufacturing Center at CMU for funding the build and materials. The authors gratefully acknowledge the help of Brian Fisher in building the samples investigated in this study, along with other help in designing the experiments. This research used resources of the Advanced Photon Source (APS), a US Department of Energy (DOE) Office of Science User Facility operated for the DOE Office of Science by Argonne National Laboratory under Contract No. DE-AC02-06CH11357. We also thank Xianghui Xiao for facilitating the  $\mu$ XCT measurements at the 2BM beamline at APS.

## References

1. R. Cunningham, S.P. Narra, T. Ozturk, J. Beuth, and A.D. Rollett, Evaluating the Effect of Processing Parameters on Porosity in Electron Beam Melted Ti-6Al-4V via Synchrotron X-ray Microtomography, *JOM*, 2016, **68**(3), p 765–771
2. J.C. Fox, S.P. Moylan, and B.M. Lane, Effect of Process Parameters on the Surface Roughness of Overhanging Structures in Laser Powder Bed Fusion Additive Manufacturing, *Proc. CIRP*, 2016, **45**, p 131–134
3. A. Vasinonta and J. Beuth, Process Maps for Controlling Residual Stress and Melt Pool Size in Laser-Based SFF Processes. in *Proceedings of 2000 Solid Freeform Fabrication Symposium*, 2000, pp. 200–208
4. J.B. Joy Gockel, Understanding Ti-6Al-4V Microstructure Control in Additive Manufacturing via Process Maps. in *Solid Freeform Fabrication Symposium*, 2013, p. 666
5. A. Cruzado et al., Multiscale Modeling of the Mechanical Behavior of IN718 Superalloy Based on Micropillar Compression and Computational Homogenization, *Acta Mater.*, 2015, **98**, p 242–253
6. Y. Tian et al., Rationalization of Microstructure Heterogeneity in INCONEL 718 Builds Made by the Direct Laser Additive Manufacturing Process, *Metall. Mater. Trans. A. Phys. Metall. Mater. Sci.*, 2014, **45**(10), p 4470–4483
7. P. Promopattum et al., Numerical Modeling and Experimental Validation of Thermal History and Microstructure for Additive Manufacturing of an Inconel 718 product, *Prog. Addit. Manuf.*, 2018, **3**, p 15–32. <https://doi.org/10.1007/s40964-018-0039-1>
8. M.B. Henderson, D. Arrell, R. Larsson, M. Heobel, and G. Marchant, Nickel Based Superalloy Welding Practices for Industrial Gas Turbine Applications, *Sci. Technol. Weld. Join.*, 2004, **9**(1), p 13–21
9. P.A. Morton, J. Mireles, H. Mendoza, P.M. Cordero, M. Benedict, and R.B. Wicker, Enhancement of Low-Cycle Fatigue Performance From Tailored Microstructures Enabled by Electron Beam Melting Additive Manufacturing Technology, *J. Mech. Des.*, 2015, **137**(11), p 111412
10. R. Cunningham, S.P. Narra, C. Montgomery, J. Beuth, and A.D. Rollett, Synchrotron-Based X-ray Microtomography Characterization of the Effect of Processing Variables on Porosity Formation in Laser Powder-Bed Additive Manufacturing of Ti-6Al-4V, *JOM.*, 2017, **69**(3), p 2–7. <https://doi.org/10.1007/s11837-016-2234-1>
11. M. Tang, P.C. Pistorius, and J.L. Beuth, Prediction of Lack-of-Fusion Porosity for Powder Bed Fusion, *Addit. Manuf.*, 2017, **14**, p 39–48
12. AMS2774E, *Heat Treatment Wrought Nickel Alloy and Cobalt Alloy Parts*. SAE International, 2016
13. ASTM E8/E8M-13, *Standard Test Methods for Tension Testing of Metallic Materials BT—Standard Test Methods for Tension Testing of Metallic Materials*. ASTM International, West Conshohocken, PA, 2013
14. ASTM E466-15, *Standard Practice for Conducting Force Controlled Constant Amplitude Axial Fatigue Tests of Metallic Materials BT—Standard Practice for Conducting Force Controlled Constant Amplitude Axial Fatigue Tests of Metallic Materials*. ASTM International, West Conshohocken, PA, 2015
15. F. De Carlo, X. Xiao, and C. Jacobsen, Research Papers TomoPy: A Framework for the Analysis of Synchrotron Tomographic Data Research Papers. 2014, pp. 1188–1193
16. E.A. Lass et al., Formation of the Ni<sub>3</sub>Nb  $\delta$ -Phase in Stress-Relieved Inconel 625 Produced via Laser Powder-Bed Fusion Additive Manufacturing, *Metall. Mater. Trans. A Phys. Metall. Mater. Sci.*, 2017, **48**(11), p 5547–5558
17. B. Farber et al., Correlation of Mechanical Properties to Microstructure in Metal Laser Sintering Inconel 718, *Mater. Sci. Eng. A*, 2018, **712**, p 539–547
18. X. Zhao, J. Chen, X. Lin, and W. Huang, Study on Microstructure and Mechanical Properties of Laser Rapid Forming Inconel 718, *Mater. Sci. Eng. A*, 2008, **478**(1-2), p 119–124